A study of the fracture behavior of unidirectional fiber-reinforced composites using Coherent Gradient Sensing (CGS) interferometry

C. LIU[1*], A.J. ROSAKIS[2], R.W. ELLIS[1] and M.G. STOUT[1]

[1]*MST-8, Materials Science and Technology Division, Los Alamos National Laboratory, Los Alamos, New Mexico 87545, U.S.A. e-mail: cliu@lanl.gov*
[2]*Graduate Aeronautical Laboratories, California Institute of Technology, Pasadena, California 91125, U.S.A.*

Abstract. The feasibility of using Coherent Gradient Sensing (CGS) interferometry for studying the fracture behavior of unidirectional fiber-reinforced composites is investigated in this paper. First, the solution for the deformation field surrounding the tip of a crack in an orthotropic material is summarized. Specifically, the most singular term in the asymptotic expansion is explicitly presented. Then, the quantities that relate to the CGS measurements are derived in terms of the spatial position, stress intensity factors, and material constants. Based on these results, synthetic CGS fringe patterns are plotted numerically, and the effects of material anisotropy and crack-tip mixity on the shape of CGS fringe pattern are investigated. In addition, a finite difference interpretation of CGS fringes caused by the finite spacing of the CGS diffraction gratings is taken into account in the simulation. Finally, the initiation fracture toughness and the subsequent resistance curve behavior of a particular unidirectional graphite/epoxy composite are measured using the CGS method. The optically measured stress intensity factors compare successfully to values obtained from the load measurements and the available analytical solutions.

Key words: Composite fracture, optical method, stress intensity factors, fracture toughness.

1. Introduction

In recent years, fiber-reinforced composite materials have been widely used in aeronautic, automotive, and other industries. It has been observed that damage develops easily in these materials under normal service loading conditions or during low-velocity impact events. Because most of the failure processes in these materials often start from crack-like defects, application of fracture mechanics to determine the toughness of fiber-reinforced composites is necessary. To develop valid theoretical models for characterizing and describing the failure process in composite materials, we first have to recognize and understand the differences of fracture processes between composites and isotropic solids. This task depends heavily on experimental observations and measurements.

To date, most of the experimental studies of composite fracture are based on mechanical techniques, where far field loads and overall deformations are measured. The near-tip parameters that really control the fracture event are inferred through numerical calibration or other indirect methods (Davis and Benzeggah, 1989; Chai, 1990; Yoon and Hong, 1990; Liu et al., 1996). On the other hand, optical techniques can be used to directly measure near-tip quantities, such as the stress intensity factors. It is now standard to use optical techniques for fracture mechanics studies of isotropic materials, where stationary cracks, statically or

---
* Author for correspondence
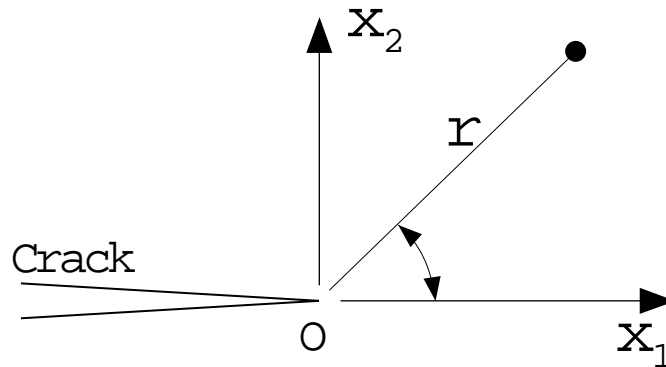
Figure 1. A semi-infinite crack in an unbounded orthotropic solid.

dynamically loaded, or even dynamically propagating cracks are considered. Nevertheless, there are few investigations of composite fracture using optical techniques. This is because the optical technique, when used in a reflection mode, requires a very high quality surface preparation–a much more difficult task for composites than homogeneous metals. Also, some optical methods, for example the method of photoelasticity, require coatings to be used on opaque solids. However, the coatings must be thick enough to generate sufficient fringes for the measurement. Meanwhile, the elastic properties of composites and the coatings can be very similar, so the deformation in the composites might be affected by the coatings.

Recently, a procedure of preparing optically reflective surfaces on composites has been developed at California Institute of Technology (Rosakis, 1994) and at Los Alamos National Laboratory. The thickness of the reflective coating is on the order of microns. As a result, it became possible to use optical techniques like the optical caustics and the Coherent Gradient Sensor (CGS) (Tippur et al., 1991; Rosakis, 1993) to study the fracture phenomenon in composite materials.

We have undertaken this study to determine the feasibility of using the CGS technique for studying the fracture of unidirectional fiber-reinforced composites. Our analysis concentrates on isolated cracks subjected to quasi-static loading, since correlations between analysis and experiments are much more accurate in this loading rate regime. We have calculated the CGS fringes that are expected for an orthotropic material, based on measured material constants, and have compared these to experimental measurements. The second validation of the CGS technique that we performed was a comparison of values of stress intensity factor at the crack tip based on the CGS fringe pattern with those derived from an analytic analysis of the specimen geometry and the measured applied load. The results of these comparisons were excellent, proving the validity of the CGS technique for orthotropic composite materials. Finally, the proposed measurement was used to obtain the quasistatic fracture toughness of the material together with its resistance curve behavior.

2. Near-tip deformation field in orthotropic solids

Consider a semi-infinite stationary crack in an unbounded homogeneous elastic orthotropic material, as shown in Figure 1. Here we focus on the situation where the direction of the crack coincides with one of the principal axes of the orthotropic solid, i.e., for a unidirectional fiber-reinforced composite, the crack is either parallel or normal to the fiber direction. A Cartesian

coordinate system is chosen such that the origin of the system is located at the crack tip and the semi-infinite crack occupies the entire negative portion of the x_1-axis. Finally, we assume that the solid undergoes planar deformation. The deformation field can be characterized by two in-plane displacement components, $u_\alpha(x_1, x_2)$, ($\alpha = 1, 2$). The in-plane components of strain are related to $u_\alpha(x_1, x_2)$ by

$$\epsilon_{\alpha\beta}(x_1, x_2) = \tfrac{1}{2}\{u_{\alpha,\beta}(x_1, x_2) + u_{\beta,\alpha}(x_1, x_2)\}, \quad \alpha, \beta \in \{1, 2\}. \tag{1}$$

2.1. CONSTITUTIVE RELATIONS

For a homogeneous elastic orthotropic material undergoing planar deformation, the generalized Hooke's law takes the following form

$$\epsilon_{11} = b_{11}\sigma_{11} + b_{12}\sigma_{22}, \qquad \epsilon_{22} = b_{21}\sigma_{11} + b_{22}\sigma_{22}, \qquad \epsilon_{12} = \tfrac{1}{2}b_{66}\sigma_{12}, \tag{2}$$

where b_{ij} are material constants and $b_{12} = b_{21}$. For planar deformation we may define three nondimensional material parameters in terms of b_{ij} as follows

$$\lambda = \frac{b_{11}}{b_{22}}, \qquad \rho = \frac{2b_{12} + b_{66}}{2\sqrt{b_{11}b_{22}}}, \qquad \kappa = \frac{3\sqrt{b_{11}b_{22}} + b_{12}}{\sqrt{b_{11}b_{22}} - b_{12}}. \tag{3}$$

Notice that for isotropic materials, λ and ρ equal 1, while $\kappa = (3 - \nu)/(1 + \nu)$ for plane-stress deformations and $\kappa = 3 - 4\nu$ for plane-strain deformations. In the degenerate case of an isotropic material, ν denotes Poisson's ratio. The positive definiteness of the strain energy density requires that

$$b_{11} > 0, \qquad b_{11}b_{22} - b_{12}^2 > 0, \qquad b_{66} > 0.$$

In terms of λ, ρ, and κ, above requirement becomes

$$\lambda > 0, \qquad \rho > -1,$$

and

$$\begin{cases} \kappa > 1, & \text{for } \rho > 1, \\ 1 < \kappa < \dfrac{3 + \rho}{1 - \rho}, & \text{for } -1 < \rho < 1. \end{cases}$$

2.2. DEFORMATION FIELD SURROUNDING THE CRACK TIP

In the absence of body force density, the equation of equilibrium is given by

$$\sigma_{\alpha\beta,\beta}(x_1, x_2) = 0, \qquad \forall (x_1, x_2) \in \overset{\circ}{\mathcal{R}}, \quad \alpha \in \{1, 2\}, \tag{4}$$

where $\overset{\circ}{\mathcal{R}} = \mathcal{R} - \mathcal{C}$, and

$$\left.\begin{aligned} \mathcal{R} &= \{(x_1, x_2) \mid -\infty < x_\alpha < \infty, \alpha = 1, 2\} \\ \mathcal{C} &= \{(x_1, x_2) \mid -\infty < x_1 \leqslant 0, x_2 = 0\} \end{aligned}\right\},$$

or $\overset{\circ}{\mathcal{R}}$ is the region of the entire two-dimensional plane except the semi-infinite line occupied by the crack.

The Airy stress function $U(x_1, x_2)$ can be defined through the following relations

$$\sigma_{11} = \frac{\partial^2 U}{\partial x_2^2}, \qquad \sigma_{22} = \frac{\partial^2 U}{\partial x_1^2}, \qquad \sigma_{12} = -\frac{\partial^2 U}{\partial x_1 \partial x_2}, \quad \forall (x_1, x_2) \in \overset{\circ}{\mathcal{R}}, \tag{5}$$

and the equilibrium Equations (4) are satisfied identically. In terms of the Airy stress function $U(x_1, x_2)$ and by using the constitutive relation (2), the requirement of compatibility becomes

$$\frac{\partial^4 U}{\partial x_1^4} + 2\rho\lambda^{1/2}\frac{\partial^4 U}{\partial x_1^2 \partial x_2^2} + \lambda\frac{\partial^4 U}{\partial x_2^4} = 0, \quad \forall (x_1, x_2) \in \overset{\circ}{\mathcal{R}}. \tag{6}$$

Suppose that the solution to (6) has the form of $U(x_1 + \mu x_2)$, where μ is an undetermined constant. Direct substitution of this form into (6) produces an equation for μ in terms of λ and ρ as follows

$$\mu^4 + 2\rho\lambda^{-1/2}\mu^2 + \lambda^{-1} = 0. \tag{7}$$

Equation (7) has no real solutions and it can be shown that for $1 \leqslant \rho < \infty$,

$$\left. \begin{array}{l} \mu_1 = i\lambda^{-1/4}\left(\sqrt{\dfrac{\rho+1}{2}} + \sqrt{\dfrac{\rho-1}{2}}\right), \mu_3 = \overline{\mu}_1 \\[4mm] \mu_2 = i\lambda^{-1/4}\left(\sqrt{\dfrac{\rho+1}{2}} - \sqrt{\dfrac{\rho-1}{2}}\right), \mu_4 = \overline{\mu}_2 \end{array} \right\}, \tag{8}$$

while for $-1 < \rho < 1$,

$$\left. \begin{array}{l} \mu_1 = \lambda^{-1/4}\left(\sqrt{\dfrac{1-\rho}{2}} + i\sqrt{\dfrac{1+\rho}{2}}\right), \mu_3 = \overline{\mu}_1 \\[4mm] \mu_2 = -\lambda^{-1/4}\left(\sqrt{\dfrac{1-\rho}{2}} - i\sqrt{\dfrac{1+\rho}{2}}\right), \mu_4 = \overline{\mu}_2 \end{array} \right\}, \tag{9}$$

where $i = \sqrt{-1}$ and the bar over a symbol stands for its complex conjugate. Now, the Airy stress function can be expressed by (Lekhnitskii, 1968)

$$U(x_1, x_2) = 2\,\text{Re}\{\phi_1(z_1) + \phi_2(z_2)\}. \tag{10}$$

In (10), $z_\alpha = x_1 + \mu_\alpha x_2$ $(\alpha = 1, 2)$, and $\phi_1(z_1)$ and $\phi_2(z_2)$ are two analytic functions. $\text{Re}\{\cdot\}$ denotes the real part of any complex expression. It should be pointed out that expression (10) is only valid for situation where $\mu_1 \neq \mu_2$. When $\rho = 1$, or $\mu_1 = \mu_2 = i\lambda^{-1/4}$, expression (10) should be replaced by

$$U(x_1, x_2) = 2\,\text{Re}\{\phi_1(z_1) + \overline{z}_1\phi_2(z_1)\}. \tag{11}$$

If, in addition, λ is also equal to 1, i.e., if the solid is isotropic, relation (11) reduces to

$$U(x_1, x_2) = 2\,\text{Re}\{\phi_1(z) + \bar{z}\phi_2(z)\}, \quad z = x_1 + ix_2. \tag{12}$$

Expression (12) has the same form as that given by Muskhelishvili (1953) for isotropic materials.

For all cases such that $\rho \neq 1$ (or $\mu_1 \neq \mu_2$), define

$$\Phi_\alpha(z_\alpha) = \phi'_\alpha(z_\alpha), \quad \alpha = 1, 2,$$

where the prime represents differentiation with respect to the complex argument. According to Lekhnitskii (1968), the stress and displacement fields inside the orthotropic solid, can be expressed in terms of $\Phi_\alpha(z_\alpha)$ as follows

$$\left.\begin{aligned}
\sigma_{11}(x_1, x_2) &= 2\,\text{Re}\{\mu_1^2\Phi'_1(z_1) + \mu_2^2\Phi'_2(z_2)\} \\
\sigma_{22}(x_1, x_2) &= 2\,\text{Re}\{\Phi'_1(z_1) + \Phi'_2(z_2)\} \\
\sigma_{12}(x_1, x_2) &= -2\,\text{Re}\{\mu_1\Phi'_1(z_1) + \mu_2\Phi'_2(z_2)\}
\end{aligned}\right\}, \quad \forall (x_1, x_2) \in \overset{\circ}{\mathcal{R}}, \tag{13}$$

and

$$\left.\begin{aligned}
u_1(x_1, x_2) &= 2\,\text{Re}\{p_1\Phi_1(z_1) + p_2\Phi_2(z_2)\} - \omega x_2 + \overset{\circ}{u}_1 \\
u_2(x_1, x_2) &= 2\,\text{Re}\{q_1\Phi_1(z_1) + q_2\Phi_2(z_2)\} + \omega x_1 + \overset{\circ}{u}_2
\end{aligned}\right\}, \quad \forall (x_1, x_2) \in \overset{\circ}{\mathcal{R}}. \tag{14}$$

In (14),

$$p_\alpha = b_{11}\left\{\mu_\alpha^2 - \frac{3-\kappa}{1+\kappa}\right\}, \qquad q_\alpha = b_{11}\left\{\frac{\lambda^{-1}}{\mu_\alpha} - \frac{3-\kappa}{1+\kappa}\mu_\alpha\right\}, \quad \alpha = 1, 2.$$

The parameter κ is defined in (3). Note that the terms associated with ω and $\overset{\circ}{u}_\alpha$ ($\alpha = 1, 2$) in (14) correspond to infinitesimal rigid body translations and rotations.

We now define the following quantities,

$$f(z) = \begin{bmatrix} \Phi_1(z) \\ \Phi_2(z) \end{bmatrix}, \qquad M = \begin{bmatrix} p_1 & p_2 \\ q_1 & q_2 \end{bmatrix}, \qquad N = \begin{bmatrix} 1 & 1 \\ \mu_1 & \mu_2 \end{bmatrix}, \tag{15}$$

where $z = x_1 + ix_2$ and we introduce two new functions $\boldsymbol{\theta}(z)$ and $\boldsymbol{\eta}(z)$ through

$$\boldsymbol{\theta}(z) = M f(z) - \overline{M}\,\overline{f}(z), \qquad \boldsymbol{\eta}(z) = N f'(z) - \overline{N}\,\overline{f}'(z), \tag{16}$$

where the bar over a symbol stands for its complex conjugate. Functions $\boldsymbol{\theta}(z)$ and $\boldsymbol{\eta}(z)$ are analytic in the entire z-plane except along the cut occupied by the crack. If there is no traction applied along the crack faces, then we have the following relations,

$$\boldsymbol{\theta}'^{\pm}(x_1) - \overline{M}\,\overline{N}^{-1}\boldsymbol{\eta}^{\pm}(x_1) + \boldsymbol{\theta}'^{\mp}(x_1) - MN^{-1}\boldsymbol{\eta}^{\mp}(x_1) = \mathbf{0}, \quad \forall x_1 < 0. \tag{17}$$

In (17), we used the notation

$$\lim_{x_2 \to 0^{\pm}} \Omega(z) = \Omega^{\pm}(x_1), \quad z = x_1 + ix_2,$$

for any analytic function $\Omega(z)$. From (17) and by posing the requirement that the displacement is bounded in the entire z-plane, one can show that $\boldsymbol{\eta}(z)$ is an entire function. As a result, the traction free condition along crack faces, (17), becomes

$$\boldsymbol{\theta}'^{+}(x_1) + \boldsymbol{\theta}'^{-}(x_1) = (\boldsymbol{M}\boldsymbol{N}^{-1} + \overline{\boldsymbol{M}}\,\overline{\boldsymbol{N}}^{-1})\boldsymbol{\eta}(x_1), \quad \forall x_1 < 0, \tag{18}$$

where $\boldsymbol{\eta}(x_1) = \boldsymbol{\eta}^{+}(x_1) = \boldsymbol{\eta}^{-}(x_1)$. Equation (18) constitutes a Riemann-Hilbert problem. By solving (18) and by considering the requirement that the stress should be bounded at infinity but can be singular at the crack tip, the general solution for the function $\boldsymbol{f}'(z)$, defined in (15), can be expressed by

$$\boldsymbol{f}'(z) = \boldsymbol{N}^{-1}\{z^{-1/2}\boldsymbol{a}(z) + \boldsymbol{b}(z)\}, \tag{19}$$

where $\boldsymbol{a}(z)$ and $\boldsymbol{b}(z)$ are two entire functions and satisfy

$$\boldsymbol{a}(z) = \overline{\boldsymbol{a}}(z), \qquad \boldsymbol{b}(z) = -\overline{\boldsymbol{b}}(z). \tag{20}$$

As we express $\boldsymbol{a}(z)$ and $\boldsymbol{b}(z)$ into their Taylor series, respectively, equation (19) provides the complete asymptotic solutions for the two functions $\Phi_1(z_1)$ and $\Phi_2(z_2)$. As in the isotropic case, the coefficients of the asymptotic expansion can only be determined through the far field loading conditions. If attention is focused on the region close to the crack tip then we may only consider the most singular solutions for $\Phi_1(z_1)$ and $\Phi_2(z_2)$. Their derivatives can be expressed as follows

$$\Phi_1'(z_1) = \frac{\mu_2 A_1 - A_2}{\mu_2 - \mu_1} \cdot \frac{1}{z_1^{1/2}}, \qquad \Phi_2'(z_2) = -\frac{\mu_1 A_1 - A_2}{\mu_2 - \mu_1} \cdot \frac{1}{z_2^{1/2}}, \tag{21}$$

where A_1 and A_2 are two arbitrary real constants. By definition, the stress intensity factors at the crack tip are given by

$$K_{\mathrm{I}} = \lim_{x_1 \to 0^{+}} \sqrt{2\pi x_1}\, \sigma_{22}(x_1, 0), \qquad K_{\mathrm{II}} = \lim_{x_1 \to 0^{+}} \sqrt{2\pi x_1}\, \sigma_{12}(x_1, 0). \tag{22}$$

As a result, the two undetermined real constants A_1 and A_2 can be related to the two stress intensity factors, K_{I} and K_{II}, through

$$A_1 = \frac{K_{\mathrm{I}}}{2\sqrt{2\pi}}, \qquad A_2 = -\frac{K_{\mathrm{II}}}{2\sqrt{2\pi}}. \tag{23}$$

Now, the expressions for $\Phi_1(z_1)$ and $\Phi_2(z_2)$ become

$$\Phi_1(z_1) = \frac{\mu_2 K_{\mathrm{I}} + K_{\mathrm{II}}}{\sqrt{2\pi}(\mu_2 - \mu_1)} z_1^{1/2}, \qquad \Phi_2(z_2) = -\frac{\mu_1 K_{\mathrm{I}} + K_{\mathrm{II}}}{\sqrt{2\pi}(\mu_2 - \mu_1)} z_2^{1/2}. \tag{24}$$

With Equation (24) in hand, the in-plane components of stress and displacement fields can be obtained by using (13) and (14).

When $\rho = 1$, or $\mu_1 = \mu_2$, we have $\mu_1 = \mu_2 = i\lambda^{-1/4}$. The Airy stress function $U(x_1, x_2)$ is provided by (11) with $z_1 = x_1 + i\lambda^{-1/4}x_2$. The stress components are then given by

$$
\left.
\begin{aligned}
\sigma_{11}(x_1, x_2) &= -2\lambda^{-1/2}\,\mathrm{Re}\{\phi_1''(z_1) - 2\phi_2'(z_1) + \overline{z}_1\phi_2''(z_1)\} \\
\sigma_{22}(x_1, x_2) &= 2\,\mathrm{Re}\{\phi_1''(z_1) + 2\phi_2'(z_1) + \overline{z}_1\phi_2''(z_1)\} \\
\sigma_{12}(x_1, x_2) &= 2\lambda^{-1/4}\,\mathrm{Im}\{\phi_1''(z_1) + \overline{z}_1\phi_2''(z_1)\}
\end{aligned}
\right\}, \quad \forall\,(x_1, x_2) \in \overset{\circ}{\mathcal{R}}, \qquad (25)
$$

and the displacement field can be expressed as

$$
\left.
\begin{aligned}
u_1(x_1, x_2) &= \frac{8b_{11}\lambda^{-1/2}}{1+\kappa}\,\mathrm{Re}\{\kappa\phi_2(z_1) - \phi_1'(z_1) - \overline{z}_1\phi_2'(z_1)\} \\
u_2(x_1, x_2) &= \frac{8b_{11}\lambda^{-3/4}}{1+\kappa}\,\mathrm{Im}\{\kappa\phi_2(z_1) + \phi_1'(z_1) + \overline{z}_1\phi_2'(z_1)\}
\end{aligned}
\right\}, \quad \forall\,(x_1, x_2) \in \overset{\circ}{\mathcal{R}}. \qquad (26)
$$

By using the similar procedure discussed above, the most singular terms in the solution of $\phi_1(z_1)$ and $\phi_2(z_1)$ can be shown to be

$$
\phi_1(z_1) = \frac{K_I + 3i\lambda^{1/4}K_{II}}{6\sqrt{2\pi}}z_1^{3/2}, \qquad \phi_2(z_1) = \frac{K_I - i\lambda^{1/4}K_{II}}{2\sqrt{2\pi}}z_1^{3/2}. \qquad (27)
$$

Where, once again, K_I and K_{II} are the mode-I and mode-II stress intensity factors at the crack tip. The complete explicit expressions for the components of the stress and displacement fields surrounding the crack tip, are given in Appendix A.

3. Application of the CGS technique to composite fracture

The Coherent Gradient Sensor (CGS) is a full field, lateral-shearing interferometric technique with an on-line filter. The physical principles governing the method of CGS were first analyzed by Tippur et al. (1991) and the technique is described in detail by Tippur (1992) and Rosakis (1993). This method, when used in a reflective mode, measures the in-plane gradients of out-of-plane surface displacements. The basic relations of the method for a reflective setup are (Rosakis, 1993),

$$
\left.
\begin{aligned}
\frac{\partial u_3(x_1, x_2)}{\partial x_1} &= \frac{mp}{2\Delta} \\
\frac{\partial u_3(x_1, x_2)}{\partial x_2} &= \frac{np}{2\Delta}
\end{aligned}
\right\}, \quad m, n = 0, \pm 1, \pm 2, \ldots, \qquad (28)
$$

where $u_3(x_1, x_2)$ is the out-of-plane displacement on the reflective surface of a specimen. In the above equation, p and Δ are the pitch and separation of the two high-density gratings, and m and n are the fringe orders for the x_1 and x_2 gradient contours, respectively. According to (28), each CGS fringe is a locus of points with the same slope in either x_1- or x_2-direction, depending on the orientation of the two high-density gratings.

3.1. GOVERNING EQUATIONS OF USING CGS TECHNIQUE IN COMPOSITE FRACTURE

For an isotropic solid subjected to plane-stress deformation, the out-of-plane displacement $u_3(x_1, x_2)$ is directly proportional to the first stress invariant. However, for an orthotropic solid, the same displacement is a more complicated function of individual normal stress components and of some of the elastic moduli. Indeed, according to the generalized Hooke's law, we have

$$\epsilon_{33} = b_{31}\sigma_{11} + b_{32}\sigma_{22} + b_{33}\sigma_{33}, \tag{29}$$

where b_{31}, b_{32}, and b_{33} are elastic constants that relate the normal stress components to the strain component normal to the (x_1, x_2)-plane. For a thin-plate specimen, plane-stress deformation condition prevails and $\sigma_{33} = 0$. Also, according to the generalized plane-stress assumption, ϵ_{33} is uniform through the specimen thickness and the out-of-plane surface displacement $u_3(x_1, x_2)$ can be related to the in-plane stress components through

$$u_3(x_1, x_2) = \frac{1}{2}\int_{-h/2}^{h/2}\epsilon_{33}\,\mathrm{d}x_3 = \tfrac{1}{2}h\{b_{31}\sigma_{11}(x_1, x_2) + b_{32}\sigma_{22}(x_1, x_2)\}, \tag{30}$$

where h is the thickness of the specimen. Near the crack tip, the most singular term dominates the deformation field. By using the result derived in the previous section for the in-plane stress components, which are listed in Appendix A, one can show that

$$\left.\begin{aligned}\frac{\partial u_3(x_1, x_2)}{\partial x_1} &= \frac{h}{4\sqrt{2\pi}}\cdot\frac{K_{\mathrm{I}}F_{11}(\theta) + K_{\mathrm{II}}F_{12}(\theta)}{r^{3/2}}\\[2mm]\frac{\partial u_3(x_1, x_2)}{\partial x_2} &= \frac{h}{4\sqrt{2\pi}}\cdot\frac{K_{\mathrm{I}}F_{21}(\theta) + K_{\mathrm{II}}F_{22}(\theta)}{r^{3/2}}\end{aligned}\right\}, \tag{31}$$

where $F_{\alpha\beta}(\theta)$ $(\alpha, \beta = 1, 2)$ are angular functions that also depend on the material constants. Their forms are given in Appendix B. In (31), we have used the notation

$$x_1 = r\,\cos\theta, \qquad x_2 = r\,\sin\theta.$$

Note that if the material becomes isotropic, then $\lambda = 1$ and $b_{31} = b_{32} = -\nu/E$, ν and E are the Poisson's ratio and Young's modulus respectively. As a result, we have

$$F_{11}(\theta) = F_{22}(\theta) = \frac{2\nu}{E}\cos\tfrac{3}{2}\theta, \qquad F_{12}(\theta) = -F_{21}(\theta) = -\frac{2\nu}{E}\sin\tfrac{3}{2}\theta,$$

and (31) becomes

$$\left.\begin{aligned}\frac{\partial u_3(x_1, x_2)}{\partial x_1} &= \frac{\nu h}{2E\sqrt{2\pi}}\cdot\frac{1}{r^{3/2}}\{K_{\mathrm{I}}\cos\tfrac{3}{2}\theta - K_{\mathrm{II}}\sin\tfrac{3}{2}\theta\}\\[2mm]\frac{\partial u_3(x_1, x_2)}{\partial x_2} &= \frac{\nu h}{2E\sqrt{2\pi}}\cdot\frac{1}{r^{3/2}}\{K_{\mathrm{I}}\sin\tfrac{3}{2}\theta + K_{\mathrm{II}}\cos\tfrac{3}{2}\theta\}\end{aligned}\right\}. \tag{32}$$

Equation (32) has the same form as that obtained by Rosakis (1993) for isotropic materials.
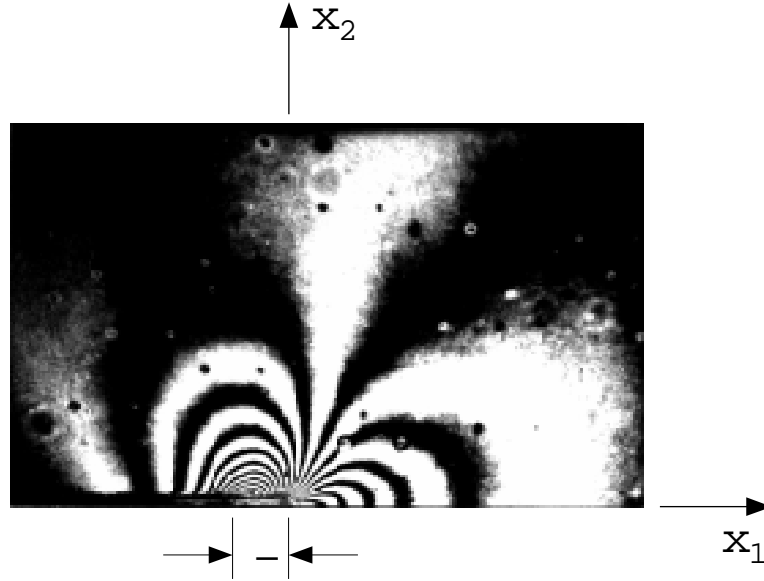
Figure 2. The CGS fringe pattern for a crack in a unidirectional fiber-reinforced composite loaded in mode-I.

Combining (28) and (31), the stress intensity factors at a stationary crack tip, K_I and K_II, can be related to the CGS fringe orders by

$$\left.\begin{aligned}
K_\mathrm{I} F_{11}(\theta) + K_\mathrm{II} F_{12}(\theta) = \frac{4\sqrt{2\pi}\, r^{3/2}}{h} \cdot \frac{mp}{2\Delta} \\[2mm]
K_\mathrm{I} F_{21}(\theta) + K_\mathrm{II} F_{22}(\theta) = \frac{4\sqrt{2\pi}\, r^{3/2}}{h} \cdot \frac{np}{2\Delta}
\end{aligned}\right\}, \quad m, n = 0, \pm 1, \pm 2, \ldots . \tag{33}$$

If we know the CGS fringe orders, m or n, and the coordinates of the point (r, θ) on the fringes, the stress intensity factors can be calculated using either of the equations in (33).

Figure 2 shows the CGS fringe pattern of a mode-I crack along the fiber direction in a unidirectional fiber-reinforced composite. The direction of the two high-density gratings is normal to the x_1-axis. Visual inspection of the fringe pattern reveals that there are two apparent crack tips separated by a distance of δ. This is due to the shearing effect of the two high-density gratings. It has been shown that (28) is valid under either of two conditions (Rosakis, 1993; Bruck and Rosakis, 1992; Bruck and Rosakis, 1993): the separation of the two high-density gratings, Δ, tends to zero, or the pitch of the grating, p, tends to infinity. In reality, both Δ and p are finite. To increase the sensitivity of the method, as required for brittle materials where out-of-plane displacement gradients are 'small', the separation, Δ, is intentionally increased. Therefore, CGS fringes should now be interpreted as finite differences of displacements. Under these circumstances, to include the effect of finite shearing, a more appropriate interpretation of the CGS fringes shown in Figure 2, is found to be (Bruck and Rosakis, 1992; Bruck and Rosakis, 1993; Lee et al., 1996)

$$\frac{u_3(x_1 + \delta, x_2) - u_3(x_1, x_2)}{\delta} = \frac{mp}{2\Delta}, \quad m = 0, \pm 1, \pm 2, \ldots . \tag{34}$$

The above relation is the accurate, 'finite' difference interpretation of CGS. The resulting CGS pattern is the superposition of the original wave front and the one which is shifted by an

amount δ (see Section 3.2). Note that as the shift $\delta \rightarrow 0$, (34) reduces to the relation of (28). A similar relation can be obtained when shifting occurs along the x_2-direction. For a complete discussion of the errors introduced by using (28) instead of (34), see Bruck and Rosakis (1992) and Bruck and Rosakis (1993).

3.2.   Numerically simulated CGS fringe patterns surrounding the crack tip in a unidirectional fiber-reinforced composite

Based on the governing Equations, (33) or (34), the CGS fringe patterns around the tip of a crack in a unidirectional fiber-reinforced composite can be simulated allowing us to visualize the features due to the material's orthotropy and crack-tip mixity. The material parameters used in this simulation are those for the graphite/epoxy unidirectional fiber-reinforced composite, IM7/8551-7 (see Table 1).

In the first simulation, using (33), we selected the orientation of the two high-density gratings to be normal to the crack. Therefore, the CGS fringes are loci of constant slope, $\partial u_3/\partial x_1$, according to Figure 1. In Figure 3 the simulated CGS fringes are presented for the situation of the crack parallel to the fibers. For this simulation, the magnitude of the complex intensity factor was held constant, i.e., $(K_I^2 + K_{II}^2)^{1/2} = 2.0$ MPa·m$^{1/2}$, and the crack-tip phase angle was stepped in 30° increments from mode-I ($\tan^{-1}(K_{II}/K_I) = 0°$) to mode-II ($\tan^{-1}(K_{II}/K_I) = 90°$). Essentially, Figures 3a, 3b and 3c have similar features except that Figures 3b and 3c are slightly asymmetric. However, Figure 3d is substantially different from the other three fringe patterns. Here, the crack-tip mixity is 90°, or the crack undergoes pure mode-II loading; while the loading component is parallel to the fibers. In Figure 3d the size of the fringes is very small compared to the purely mode-I case of the same stress intensity factor magnitude. In addition, there seems to be a sudden, almost discontinuous, change from mixed-mode loading to pure mode-II loading for the case of a crack parallel to the fibers.

In Figure 4 the simulated CGS fringes for a crack normal to the fibers are presented. All other conditions are the same as for the previous case whose results were presented in Figure 3. In Figure 4a, the crack is subjected to mode-I loading parallel to the fiber direction. The fringe loops are very small and kinks in the fringes can be seen. Surprisingly, the fringe patterns shown in Figures 4b, 4c, and 4d, have similar orientations and features. Only the size of the fringes increases as the magnitude of the mode-II loading component becomes larger. We conclude, combining observations from the simulations shown in Figures 3 and 4, that for a crack in an orthotropic material, the shape of the CGS fringes is controlled by the loading component parallel to the 'soft' direction. In Figure 3, this is the mode-I component and in Figure 4, this is the mode-II component. Whenever the loading component parallel to the 'soft' direction is nonzero, the shapes of the CGS fringes look similar. However, the size of the fringes are proportional to the magnitude of the loading component in the 'soft' direction. The loading component that is parallel to the 'stiff' direction (the fibers) does not contribute much to the CGS fringe patterns.

The characteristics of the CGS fringe patterns in isotropic materials, under mixed-mode loading conditions, have been discussed by Mason et al. (1992). For isotropic solids, the fringe loops, corresponding to the same stress intensity factor magnitude, have identical shapes and sizes, irrespective of mode mixity. The only difference between patterns is a rotation depending on mode mixity. Also, each set of loops has its own axis of symmetry emanating from the
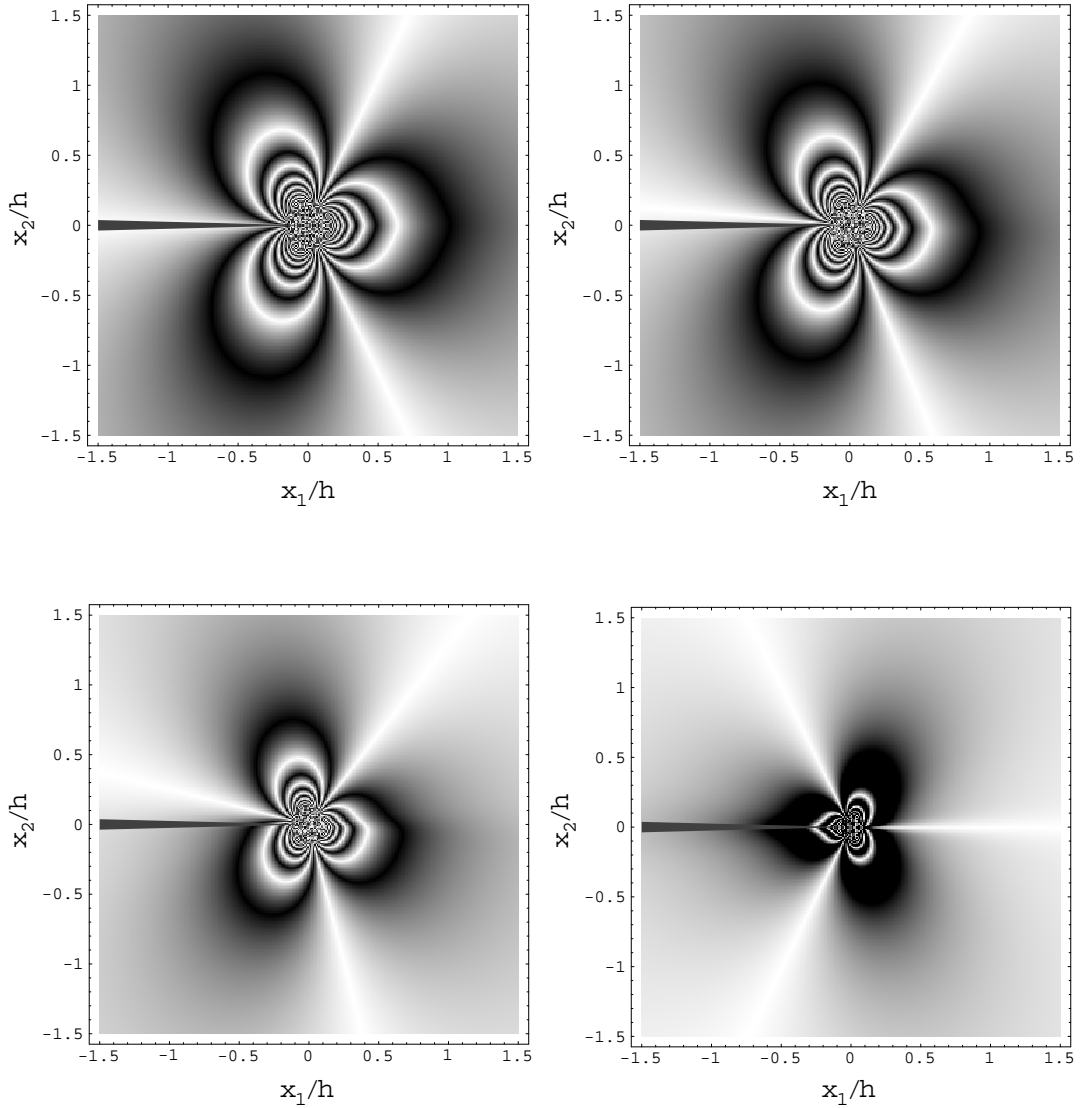
Figure 3. Simulated CGS fringe patterns of a crack parallel to the fibers in a unidirectional fiber-reinforced composite. For the conditions of $(K_I^2 + K_{II}^2)^{1/2} = 2.0\,\text{MPa·m}^{1/2}$; (a) $\tan^{-1}(K_{II}/K_I) = 0°$; (b) $\tan^{-1}(K_{II}/K_I) = 30°$; (c) $\tan^{-1}(K_{II}/K_I) = 60°$; (d) $\tan^{-1}(K_{II}/K_I) = 90°$.

crack tip. These axes are 120° apart. When the crack-tip mixity changes, the three fringe loops simply rotate with respect to the crack tip. Due to the material's orthotropy, these features no longer exist for the crack in the unidirectional fiber-reinforced composite.

In the CGS optical setup, two line diffraction gratings of fine pitch p are used. They are spaced a distance Δ apart to perform a shearing of the incident wave front. If only the $+1$ or -1 diffraction order is considered, the diffraction angle, θ, is

$$\theta = \sin^{-1}\frac{\ell}{p} \approx \frac{\ell}{p}, \tag{35}$$
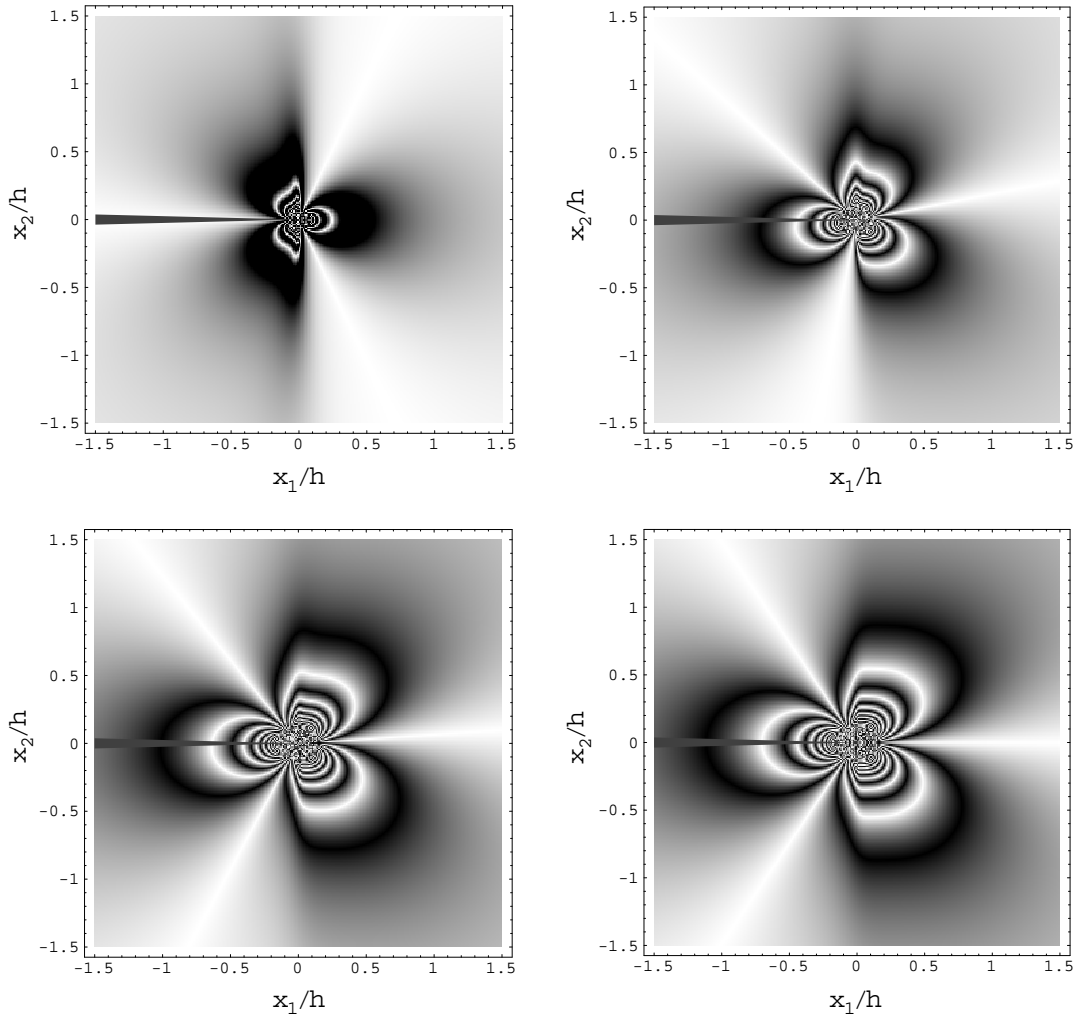
Figure 4. Simulated CGS fringe patterns of a crack normal to the fibers in a unidirectional fiber-reinforced composite. For the conditions of $(K_I^2 + K_{II}^2)^{1/2} = 2.0\,\mathrm{MPa \cdot m}^{1/2}$; (a) $\tan^{-1}(K_{II}/K_I) = 0°$; (b) $\tan^{-1}(K_{II}/K_I) = 30°$; (c) $\tan^{-1}(K_{II}/K_I) = 60°$; (d) $\tan^{-1}(K_{II}/K_I) = 90°$.

where ℓ is the wavelength of the light. The resulting CGS image is the superposition of the original wavefront and the one which has been shifted by an amount δ. Then the quantity δ is related to Δ, the separation of the two gratings, through

$$\delta = \Delta \, \tan \theta \approx \Delta \left(\frac{\ell}{p} \right). \tag{36}$$

Thus, the amount of shift, δ, is proportional to the grating separation distance Δ. In Figure 5, simulations based on (34) are shown. They illustrate the effect of the finite shift δ on the CGS fringe patterns. Consider the case of a crack parallel to the fibers and subjected to a mode-I loading condition. Figure 5 presents the simulated CGS fringes for different amounts of relative shift δ/h where h is the specimen thickness. The two virtual crack tips are obvious in these simulations, especially when the relative shifting amount δ/h approaches unity. From
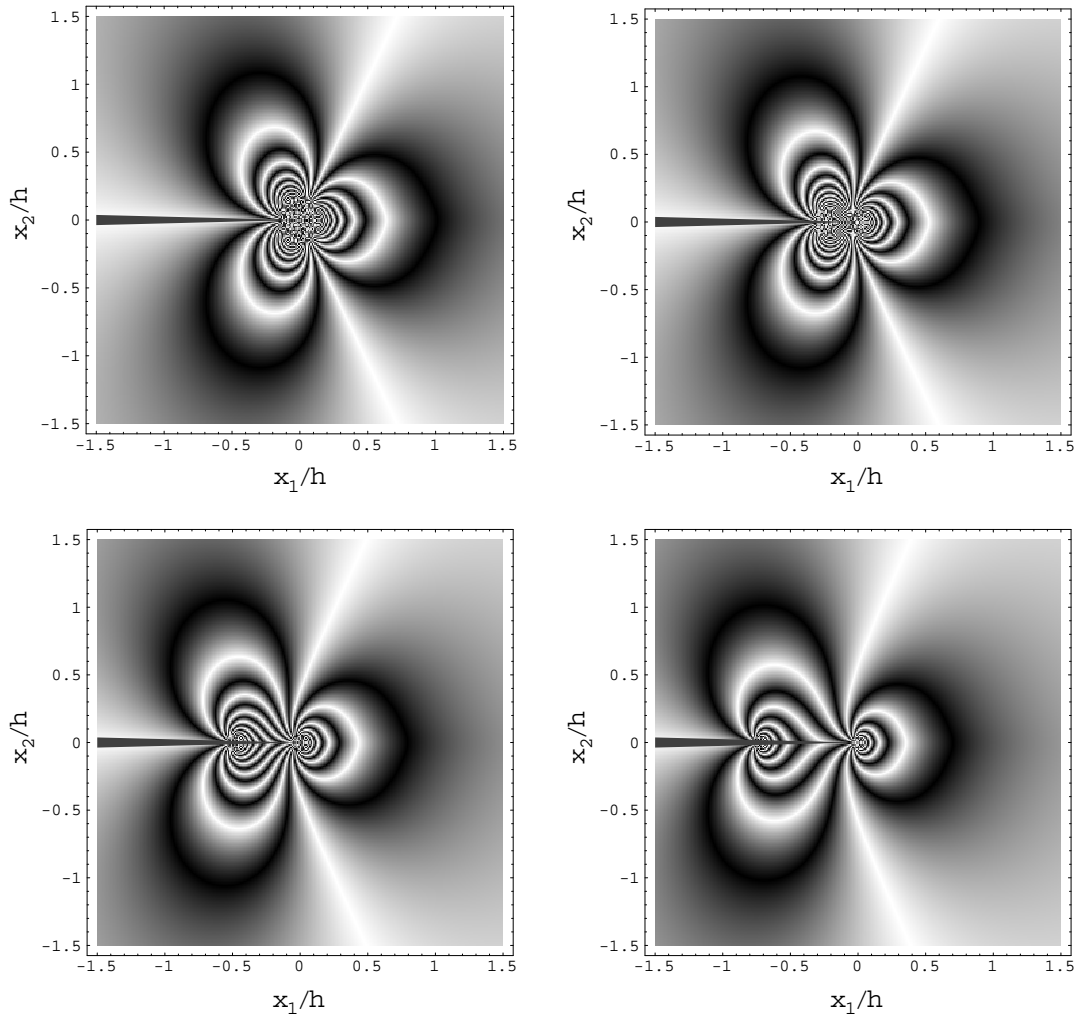
Figure 5. Simulated CGS fringe patterns of a crack parallel to the fibers in a unidirectional fiber-reinforced composite. For the conditions of $K_I = 2.0$ MPa·m$^{1/2}$ and $K_{II} = 0$, and (a) $\delta/h = 0.0$; (b) $\delta/h = 0.25$; (c) $\delta/h = 0.50$; (d) $\delta/h = 0.75$; where h is the thickness of the specimen.

these observations, and by comparing the simulations shown in Figure 5 with the photograph in Figure 2, we recognized the necessity to consider δ as an extra parameter to be extracted from the image, just like the two stress intensity factors, K_I and K_{II}. The numerical scheme to obtain the stress intensity factors and the finite shift, δ, will be discussed in the next section.

4. Stress intensity factor measurement from the IM7/8551-7 graphite/epoxy composite

Based on the analysis presented in the previous sections, the stress intensity factor and associated fracture toughness at the tip of a crack in a graphite/epoxy unidirectional fiber-reinforced composite are measured using the CGS technique. Issues related to the experimental measurement are discussed in this section and the experimental results are compared with available analytical solutions.
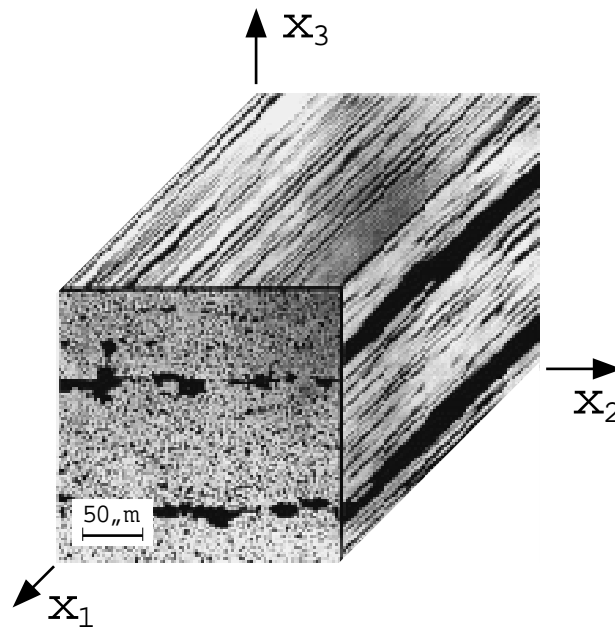
Figure 6. Micrographs of the graphite/epoxy unidirectional fiber-reinforced composite, IM7/8551-7.
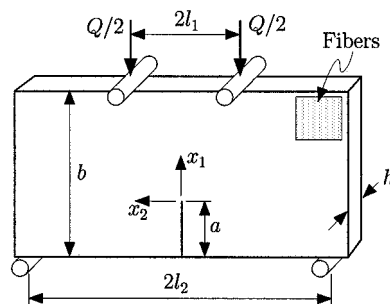
Figure 7. Four-point-bend specimen with a single edge crack.

4.1. COMPOSITE MATERIAL AND SPECIMEN PREPARATION

A unidirectional graphite/epoxy composite, IM7/8551-7, was used in this experimental study. This composite material was obtained from Hercules Advanced Materials and Systems Company. The microstructure of the unidirectional composite is shown in Figure 6, a collection of optical micrographs showing the three orthogonal material orientations. The diameter of the continuous fibers is approximately 5 μm and the thickness of a lamina is on the order of 100 μm. The fiber volume fraction is approximately 60 percent; it might be noted that the matrix is a rubber-toughened (mean particle size 10–75 μm) epoxy.

A Cartesian coordinate system has been chosen such that the x_1-axis is along the fiber direction, the x_2-axis lies in the laminate plane and normal to the fibers, and the x_3-axis is normal to the laminate plane. Since the material, shown in Figure 6, is symmetric with respect to the three coordinate planes it can be modeled as an orthotropic solid, and (x_1, x_2, x_3) are the principal axes of the material. The elastic constants of the unidirectional graphite/epoxy

Table 1. Material elastic constants

	E_{11}	E_{22}	E_{33}
Young's moduli (GPa)	148.60	8.40	8.28
	μ_{12}	μ_{23}	μ_{13}
Shear moduli (GPa)	5.45	3.03	4.34
	ν_{12}	ν_{23}	ν_{13}
Poisson's ratios	0.32	0.37	0.35

composite have been measured with respect to the principal axes (x_1, x_2, x_3), and the results are listed in Table 1.

The specimen geometry we chose for this experimental study was the four-point-bend specimen with a single-edge precrack, as shown in Figure 7. The specimens used in the experiment were cut from a 6.5 mm thick IM7/8551-7 graphite/epoxy unidirectional composite plate. The nominal dimensions of the specimen, shown in Figure 7, are: $2l_1 = 75$ mm, $2l_2 = 125$ mm, $b = 75$ mm, $h = 6.5$ mm, and $a = 25$ mm. A diamond saw, with thickness of 0.254 mm, was used to cut the precrack in the specimen. A cut was made from each side of the specimen, which left a chevron at the end of the slot. A hand saw was then used to cut out the chevron, and finally, a surgical blade was used to sharpen the tip of the precrack. An Instron load frame was used to load the sample with a total applied force of Q. In this experimental study, we concentrate on the situation where the crack is parallel to the fibers and the specimen plane is parallel to the laminates. A Cartesian coordinate system is chosen with the origin located at the crack tip. The axes of this system are aligned with the principal axes of the orthotropic material. In this coordinate system, the two nondimensional material parameters are $\lambda = 0.0565$ and $\rho = 3.1676$. The third nondimensional parameter κ does not appear in the process of CGS fringe analysis. The two elastic constants, b_{31} and b_{32} that appeared in (29) and (30), are given by $b_{31} = -\nu_{13}/E_{11}$ and $b_{32} = -\nu_{23}/E_{22}$, respectively.

As we have mentioned earlier, a very high quality surface preparation is required in order to apply the CGS technique to composite materials. However, because of the microstructure of the composite material, we cannot polish the specimen surface to make it optically flat, neither can we directly deposit a reflective aluminum film on the specimen by vacuum deposition. We have recently developed a procedure of preparing an optically flat and reflective surface on composites. An optically flat glass is coated with a thin aluminum film having a thickness of only several angstroms. A layer of segregation material is intentionally maintained between the coating and the glass, to prevent bonding between the aluminum film and the glass. This material was the residue of liquid soap used to clean the glass. The coated glass is then combined with the sample using an epoxy adhesive to glue the coated surface of the optically flat glass to the sample. The epoxy adhesive was PC-1 Bipax of epoxy resin and diethylenetriamine hardener obtained from the Photoelastic Division, Measurements Group, Inc., Raleigh, NC. After the epoxy has cured, the glass is peeled off. Because the bond between the aluminum film and the glass is very weak, the aluminum coating is transferred onto the

Figure 8. CGS fringe pattern surrounding the crack tip in the IM7/8551-7 unidirectional fiber-reinforced composite.

sample surface. The total thickness of the epoxy layer and the coating is just a couple of microns. Compared with the sample thickness, this layer is very thin and will not affect the deformation state inside the specimen.

4.2. EXPERIMENTAL OBSERVATIONS

The four-point-bend specimen was loaded using an Instron screw-driven load frame by displacement control to enhance crack-tip stability. A 50 mm-diameter collimated He-Ne laser beam (wave length = 632 nm) was roughly centered around the crack tip reflecting from the aluminized specimen surface. Two high-density gratings were positioned in the reflected beam and the gratings are perpendicular to the crack. Therefore, information regarding the quantity $\partial u_3/\partial x_1$ was obtained. The grating pitch was $p = 0.025$ mm. In order to increase the sensitivity, the distance between the two high-density gratings was set at $\Delta = 100$ mm. The corresponding fringe sensitivity for this grating separation was approximately 0.007°/fringe. As the load increases, the stress field near the crack tip continuously builds up and the CGS fringes also enlarge continuously. The interference fringes surrounding the crack tip were recorded by a motor-driven 35 mm camera and the corresponding load was also recorded at each exposure. Figure 8 shows one of the recorded photographs. Clearly, the photographed fringe patterns are qualitatively similar to the simulation results discussed in the previous section. The similarity between the simulated fringe pattern and the photograph suggests that the stress intensity factor can be considered as the controlling parameter characterizing the fracture behavior of the fiber-reinforced composite. Recall that the simulated CGS fringe patterns were indeed based on the assumption that a K-dominant region surrounding the crack tip exists. Well above the crack tip, one can see that the fringes are no longer symmetric about the crack axis. This is because the composite plate, as it is received, is not completely flat.

Another feature that is observed from the photograph is that there are two apparent crack tips. This is due to the large distance, Δ, between the two high-density gratings and the resulting relatively large shift, δ, between the two interfering beams. Therefore, (33) cannot be used in the CGS fringes interpretation because it assumes that the image shifting is infinitesimal. Instead we have to use (34) for data analysis. We treat δ as an additional unknown parameter in the CGS fringes interpretation process, because (36) only provides an estimation for the shift δ and the measurement of δ directly from the photograph is inaccurate. The procedure for obtaining the stress intensity factors at the crack tip will be discussed next.

4.3. CGS FRINGE INTERPRETATION

To obtain the stress intensity factor at the crack tip, the photograph of the CGS fringe patterns was first digitized. According to the analyses of Rosakis and Ravi-Chandar (1986) and Krishnaswamy et al. (1992), data points must be chosen at a distance from the crack tip greater than half of the specimen thickness, to avoid the influence of three-dimensional effects. A least squares scheme was used to fit the experimental data to expression (34) to obtain the parameters K_I, K_{II}, and δ. However, since the dependence of the out-of-plane displacement u_3 on the parameter δ is not linear, the least squares scheme also becomes nonlinear. We use the over-deterministic method developed by Sanford and Dally (1979) to determine the unknown parameters. The fitting process involves both the Newton-Raphson method and the minimization process associated with the least squares procedure.

For each data point (x_1^i, x_2^i) and the associated fringe order m^i, we define

$$f_i(K_I, K_{II}, \delta) = \left\{ \frac{u_3(x_1^i + \delta, x_2^i) - u_3(x_1^i, x_2^i)}{\delta} - \frac{m^i p}{2\Delta} \right\}^2, \quad i = 1, 2, \ldots, n, \tag{37}$$

where n is the total number of data points. Suppose that K_I^j, K_{II}^j, and δ^j are the estimates of the unknown parameters in the jth iteration. Then in the $(j+1)$th iteration step, we have

$$f_i^{j+1} = f_i^j + \left(\frac{\partial f_i}{\partial K_I}\right)^j \Delta K_I + \left(\frac{\partial f_i}{\partial K_{II}}\right)^j \Delta K_{II} + \left(\frac{\partial f_i}{\partial \delta}\right)^j \Delta\delta, \quad i = 1, 2, \ldots, n. \tag{38}$$

By introducing

$$\boldsymbol{f} = \begin{bmatrix} f_1 \\ f_2 \\ \cdots \\ f_n \end{bmatrix}, \qquad \boldsymbol{A} = \begin{bmatrix} \dfrac{\partial f_1}{\partial K_I} & \dfrac{\partial f_1}{\partial K_{II}} & \dfrac{\partial f_1}{\partial \delta} \\ \dfrac{\partial f_2}{\partial K_I} & \dfrac{\partial f_2}{\partial K_{II}} & \dfrac{\partial f_2}{\partial \delta} \\ \cdots & \cdots & \cdots \\ \dfrac{\partial f_n}{\partial K_I} & \dfrac{\partial f_n}{\partial K_{II}} & \dfrac{\partial f_n}{\partial \delta} \end{bmatrix}, \qquad \boldsymbol{k} = \begin{bmatrix} \Delta K_I \\ \Delta K_{II} \\ \Delta\delta \end{bmatrix},$$

Equation (38) has the form

$$\boldsymbol{f}^{j+1} = \boldsymbol{f}^j + \boldsymbol{A}^j \boldsymbol{k}, \quad j = 0, 1, 2, \ldots. \tag{39}$$

In addition, by requiring that $\boldsymbol{f}^{j+1} = \boldsymbol{0}$, we have

$$\boldsymbol{k} = -(\boldsymbol{C}^j)^{-1} \boldsymbol{b}^j, \qquad \boldsymbol{C}^j = (\boldsymbol{A}^j)^\top (\boldsymbol{A}^j), \qquad \boldsymbol{b}^j = (\boldsymbol{A}^j)^\top \boldsymbol{f}^j, \tag{40}$$

which gives the correction factor $\boldsymbol{k}$ for the $(j+1)$th iteration. The value of the fitting parameters at the $(j+1)$th iteration is given by

$$(K_I^{j+1}, K_{II}^{j+1}, \delta^{j+1})^\top = (K_I^j, K_{II}^j, \delta^j)^\top + \boldsymbol{k}, \quad j = 0, 1, 2, \ldots. \tag{41}$$

This iterative procedure can be repeated until $|\boldsymbol{k}| \leqslant \epsilon$, where ϵ is the measure of prescribed error tolerance.
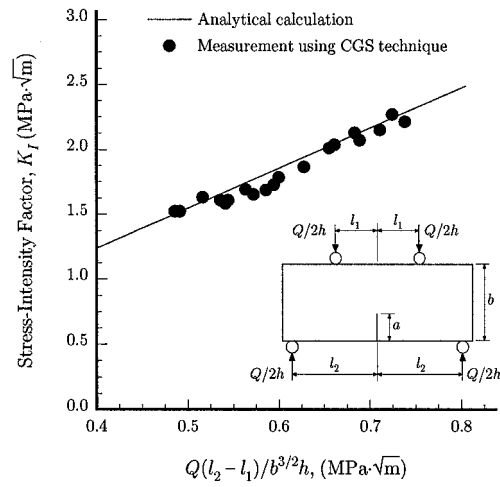
Figure 9. Comparison of the CGS experimental measurement with the results of analytic solution.

Because this iteration procedure is nonlinear, the choice of the initial value will affect the convergence of the process. For our tests, the following approach was used to obtain the initial value $(K_{\mathrm{I}}^0, K_{\mathrm{II}}^0, \delta^0)^\top$. We first used the linear least squares scheme to fit the experimental data to expression (33), thus obtaining the two values for K_{I}^0 and K_{II}^0. The value δ^0 was next estimated from the photograph. With the accuracy of $\epsilon = 0.1$ percent, convergence of the iterative process was then achieved within 10 steps.

4.4. Comparison with analytical calculations

To assess the accuracy of using the optical CGS technique to obtain the stress intensity factor at a crack tip for the graphite/epoxy fiber-reinforced composite, the experimental CGS measurement was compared with an available analytical solution. This is an extension of an existing solution corresponding to isotropic materials. For the specimen geometry and loading configuration depicted in Figure 7, the stress intensity factor at the crack tip is given by

$$K_{\mathrm{I}} = \sigma\sqrt{\pi a} \cdot F\left(\frac{a}{b}\right) Y(\rho), \qquad \sigma = \frac{3Q}{b^2 h}(l_2 - l_1), \tag{42}$$

where $Y(\rho)$ is a function of the nondimensional material parameter ρ, as defined previously. Function $Y(\rho)$ has been approximated by Bao et al., (1992) by a polynomial form,

$$Y(\rho) = \sqrt{\frac{1+\rho}{2}}\{1 + 0.1(\rho - 1) - 0.016(\rho - 1)^2 + 0.002(\rho - 1)^3\}, \tag{43}$$

with an error of less than 2 percent. Also note that $Y(1) = 1$. The dependence of the function $F(a/b)$ on the specimen geometry is discussed in Appendix C. $F(a/b)$ is the same as for an isotropic specimen subjected to four-point-bend loading. In Figure 9, the stress intensity factor measured using the CGS technique is compared to that obtained with the analytical solution. The agreement between the analytical solution and the optical experimental measurement is excellent.
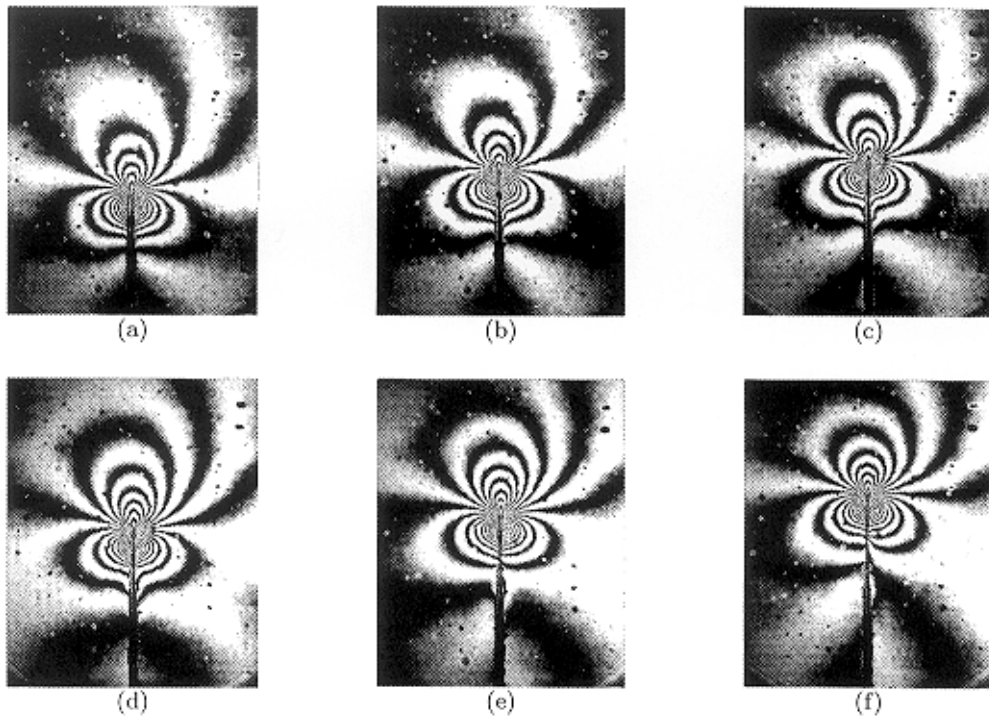
Figure 10. CGS fringe patterns showing stable crack growth under quasi-static loading.
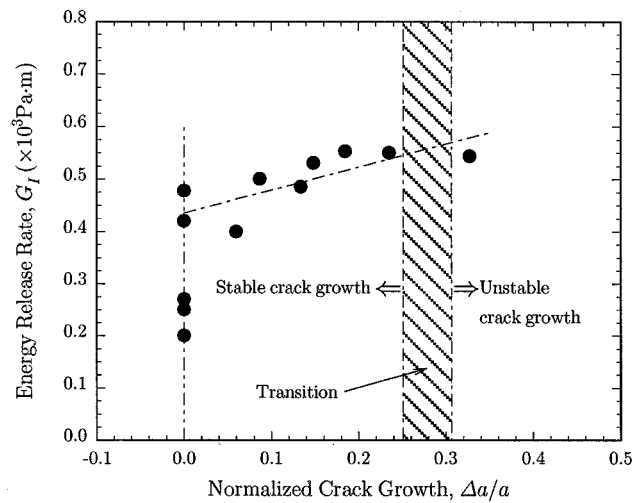
Figure 11. Measured energy-release rate as a function of crack growth during the process of stable propagation.

4.5. INITIATION TOUGHNESS UNDER QUASI-STATIC LOADING

In our four-point-bend experiment, the applied load was monitored during the test. The load was a linearly increasing function of the deflection before it reached the maximum value. The specimen failed catatrophically at the maximum load. Once the crack initiated, it propagated unstably. Therefore, from the load/deflection behavior, the specimen fractured in a brittle manner. However, a very small amount of stable crack growth was indeed observed and captured

using the optical CGS technique together with the motor-driven camera. We believe this small amount of stable crack growth is due to the rubber-toughened phase in the epoxy matrix. Some selected CGS photographs showing the stable crack growth, are presented in Figure 10. Here, we need to point out that the photographs shown in Figure 10 were taken in a very short period of time by the motor-driven camera. It shows that CGS can capture the phenomenon which might be overlooked due to the overall brittleness of the process. Another advantage of using optical methods to study the process of fracture is that the position of the crack tip can be measured accurately. The measured energy-release rate G_I as a function of crack growth is shown in Figure 11. Here we have used the relation between the energy-release rate G_I and the mode-I stress intensity factor K_I given by Hutchinson and Suo (1992),

$$G_I = \lambda^{-3/4} \sqrt{\frac{1+\rho}{2}} \cdot \frac{K_I^2}{E_{11}}, \tag{44}$$

where E_{11} is the Young's modulus along the fiber direction listed in Table 1. Close to the point of stable initiation of the stationary crack, the energy-release rate is higher than the value of the growing crack. This is because the initial stationary crack tip has a finite radius (~ 0.1 mm). However, once the crack starts to propagate, the energy-release rate value will correspond to the sharp crack. Accordingly, the fracture initiation toughness was determined by back extrapolating the G_I data of the stably growing crack. From Figure 11, we estimated the initiation toughness of a sharp crack to be 0.44×10^3 Pa·m which is consistent with the measurements made by Hercules.

5. Concluding remarks

In this study we have demonstrated that the Coherent Gradient Sensor (CGS) technique can be used to measure the fracture toughness and critical strain-energy release rates of orthotropic low toughness materials (unidirectional graphite/epoxy composite) under the plane-stress deformation condition. Our measurements of stress intensity factor using the CGS approach compared favorably with values determined using an analytic solution. In addition, the appearance of fringes calculated on the basis of a K-dominant crack-tip field, were in good agreement with photographic fringe records obtained using the CGS method, thus proving the validity of this necessary assumption. Finally, our measurement of fracture initiation toughness using the CGS experimental fringe patterns agrees well with other independent measurements. In summary, the CGS method is capable of quantifying the near-tip parameters that control the fracture process for unidirectional graphite/epoxy composite materials.

The CGS technique has many advantages for studying fracture events. It is a noncontact technique that can provide a continuous record of the fracture initiation and propagation. Although the present work was performed at quasi-static loading rates, all of the adopted methodologies are also applicable to dynamic loading and to fast crack growth events. In such cases the CGS technique can also be used to measure fracture toughness parameters associated with dynamic failure. Indeed, when the loading and subsequent crack growth take place in very short times (hundreds of microseconds), boundary value measurements are incapable of providing meaningful information regarding fracture behavior. In such cases optical methods, such as CGS, are the only alternative.

Appendix

A. Deformation field surrounding the crack tip

In this Appendix, the K-dominant components of the stress and the displacement fields surrounding a stationary crack tip in an orthotropic solid are provided in terms of the nondimensional material parameters λ, ρ, κ, and the stress intensity factors K_{I} and K_{II}. Three different cases for the parameter ρ are considered:

(i) $\rho > 1$,

(ii) $-1 < \rho < 1$, and

(iii) $\rho = 1$.

According to the definition given in Section 2.1, we always have $\lambda > 0$. Also we assign (r, θ) to be the polar coordinates centered at the crack tip.

For $\rho > 1$, the most singular stress components are

$$
\left.
\begin{aligned}
\sigma_{11} &= \frac{K_{\text{I}}}{\sqrt{2\pi}} \cdot \frac{\lambda^{-1/2}}{\rho_+ - \rho_-} \{\rho_+ r_1^{-1/2} \cos \tfrac{1}{2}\theta_1 - \rho_- r_2^{-1/2} \cos \tfrac{1}{2}\theta_2\} \\
&\quad - \frac{K_{\text{II}}}{\sqrt{2\pi}} \cdot \frac{\lambda^{-1/4}}{\rho_+ - \rho_-} \{\rho_+^2 r_1^{-1/2} \sin \tfrac{1}{2}\theta_1 - \rho_-^2 r_2^{-1/2} \sin \tfrac{1}{2}\theta_2\}, \\
\sigma_{22} &= -\frac{K_{\text{I}}}{\sqrt{2\pi}} \cdot \frac{1}{\rho_+ - \rho_-} \{\rho_- r_1^{-1/2} \cos \tfrac{1}{2}\theta_1 - \rho_+ r_2^{-1/2} \cos \tfrac{1}{2}\theta_2\} \\
&\quad + \frac{K_{\text{II}}}{\sqrt{2\pi}} \cdot \frac{1}{\lambda^{-1/4}(\rho_+ - \rho_-)} \{r_1^{-1/2} \sin \tfrac{1}{2}\theta_1 - r_2^{-1/2} \sin \tfrac{1}{2}\theta_2\}, \\
\sigma_{12} &= \frac{K_{\text{I}}}{\sqrt{2\pi}} \cdot \frac{\lambda^{-1/4}}{\rho_+ - \rho_-} \{r_1^{-1/2} \sin \tfrac{1}{2}\theta_1 - r_2^{-1/2} \sin \tfrac{1}{2}\theta_2\} \\
&\quad + \frac{K_{\text{II}}}{\sqrt{2\pi}} \cdot \frac{1}{\rho_+ - \rho_-} \{\rho_+ r_1^{-1/2} \cos \tfrac{1}{2}\theta_1 - \rho_- r_2^{-1/2} \cos \tfrac{1}{2}\theta_2\}
\end{aligned}
\right\} \tag{45}
$$

and the displacement field is given by

$$
\begin{aligned}
u_1 &= \frac{K_{\mathrm{I}}}{\sqrt{2\pi}} \cdot \frac{2b_{11}\lambda^{-1/2}}{\rho_+ - \rho_-} \left\{ \left(\rho_+^2 + \frac{3-\kappa}{1+\kappa} \right) \rho_- r_1^{1/2} \cos \tfrac{1}{2}\theta_1 \right. \\
&\qquad\qquad \left. - \left(\rho_-^2 + \frac{3-\kappa}{1+\kappa} \right) \rho_+ r_2^{1/2} \cos \tfrac{1}{2}\theta_2 \right\} \\
&\quad + \frac{K_{\mathrm{II}}}{\sqrt{2\pi}} \cdot \frac{2b_{11}\lambda^{-1/4}}{\rho_+ - \rho_-} \left\{ \left(\rho_+^2 + \frac{3-\kappa}{1+\kappa} \right) r_1^{1/2} \sin \tfrac{1}{2}\theta_1 \right. \\
&\qquad\qquad \left. - \left(\rho_-^2 + \frac{3-\kappa}{1+\kappa} \right) r_2^{1/2} \sin \tfrac{1}{2}\theta_2 \right\}, \\
u_2 &= -\frac{K_{\mathrm{I}}}{\sqrt{2\pi}} \cdot \frac{2b_{11}\lambda^{-3/4}}{\rho_+ - \rho_-} \left\{ \left(\rho_- + \frac{3-\kappa}{1+\kappa}\rho_+ \right) \rho_- r_1^{1/2} \sin \tfrac{1}{2}\theta_1 \right. \\
&\qquad\qquad \left. - \left(\rho_+ + \frac{3-\kappa}{1+\kappa}\rho_- \right) \rho_+ r_2^{1/2} \sin \tfrac{1}{2}\theta_2 \right\} \\
&\quad + \frac{K_{\mathrm{II}}}{\sqrt{2\pi}} \cdot \frac{2b_{11}\lambda^{-1/2}}{\rho_+ - \rho_-} \left\{ \left(\rho_- + \frac{3-\kappa}{1+\kappa}\rho_+ \right) r_1^{1/2} \cos \tfrac{1}{2}\theta_1 \right. \\
&\qquad\qquad \left. - \left(\rho_+ + \frac{3-\kappa}{1+\kappa}\rho_- \right) r_2^{1/2} \cos \tfrac{1}{2}\theta_2 \right\},
\end{aligned}
\tag{46}
$$

where

$$
\begin{aligned}
&\rho_\pm = \sqrt{\frac{\rho+1}{2}} \pm \sqrt{\frac{\rho-1}{2}}, \\
&r_{1,2} = r\{\cos^2\theta + \lambda^{-1/2}\rho_\pm^2 \sin^2\theta\}^{1/2}, \qquad \theta_{1,2} = \tan^{-1}\{\lambda^{-1/4}\rho_\pm \tan\theta\}.
\end{aligned}
$$

For $-1 < \rho < 1$, the most singular stress components are

$$
\begin{aligned}
\sigma_{11} &= \frac{K_{\mathrm{I}}}{\sqrt{2\pi}} \cdot \frac{\lambda^{-1/2}}{2\cos\alpha}\{r_1^{-1/2}\cos(\tfrac{1}{2}\theta_1 - \alpha) + r_2^{-1/2}\cos(\tfrac{1}{2}\theta_2 + \alpha)\} \\
&\quad - \frac{K_{\mathrm{II}}}{\sqrt{2\pi}} \cdot \frac{\lambda^{-1/4}}{2\cos\alpha}\{r_1^{-1/2}\cos(\tfrac{1}{2}\theta_1 - 2\alpha) - r_2^{-1/2}\cos(\tfrac{1}{2}\theta_2 + 2\alpha)\}, \\
\sigma_{22} &= \frac{K_{\mathrm{I}}}{\sqrt{2\pi}} \cdot \frac{1}{2\cos\alpha}\{r_1^{-1/2}\cos(\tfrac{1}{2}\theta_1 + \alpha) + r_2^{-1/2}\cos(\tfrac{1}{2}\theta_2 - \alpha)\} \\
&\quad - \frac{K_{\mathrm{II}}}{\sqrt{2\pi}} \cdot \frac{1}{2\lambda^{-1/4}\cos\alpha}\{r_1^{-1/2}\cos\tfrac{1}{2}\theta_1 - r_2^{-1/2} - \cos\tfrac{1}{2}\theta_2\}, \\
\sigma_{12} &= -\frac{K_{\mathrm{I}}}{\sqrt{2\pi}} \cdot \frac{\lambda^{-1/4}}{2\cos\alpha}\{r_1^{-1/2}\cos\tfrac{1}{2}\theta_1 - r_2^{-1/2}\cos\tfrac{1}{2}\theta_2\} \\
&\quad + \frac{K_{\mathrm{II}}}{\sqrt{2\pi}} \cdot \frac{1}{2\cos\alpha}\{r_1^{-1/2}\cos(\tfrac{1}{2}\theta_1 - \alpha) + r_2^{-1/2}\cos(\tfrac{1}{2}\theta_2 + \alpha)\}
\end{aligned}
\tag{47}
$$

and the displacement field is

$$
\left.
\begin{aligned}
u_1 &= \frac{K_{\mathrm{I}}}{\sqrt{2\pi}} \cdot \frac{b_{11}\lambda^{-1/2}}{\cos\alpha} \left\{ r_1^{1/2}\left[\cos(\tfrac{1}{2}\theta_1+\alpha)-\frac{3-\kappa}{1+\kappa}\cos(\tfrac{1}{2}\theta_1-\alpha)\right]\right.\\
&\qquad\qquad\qquad\qquad \left. +r_2^{1/2}\left[\cos(\tfrac{1}{2}\theta_2-\alpha)-\frac{3-\kappa}{1+\kappa}\cos(\tfrac{1}{2}\theta_2+\alpha)\right]\right\}\\
&\quad -\frac{K_{\mathrm{II}}}{\sqrt{2\pi}}\cdot\frac{b_{11}\lambda^{-1/4}}{\cos\alpha}\left\{ r_1^{1/2}\left[\cos(\tfrac{1}{2}\theta_1+2\alpha)-\frac{3-\kappa}{1+\kappa}\cos\tfrac{1}{2}\theta_1\right]\right.\\
&\qquad\qquad\qquad\qquad \left. -r_2^{1/2}\left[\cos(\tfrac{1}{2}\theta_2-2\alpha)-\frac{3-\kappa}{1+\kappa}\cos\tfrac{1}{2}\theta_2\right]\right\},\\
u_2 &= \frac{K_{\mathrm{I}}}{\sqrt{2\pi}}\cdot\frac{b_{11}\lambda^{-3/4}}{\cos\alpha}\left\{ r_1^{1/2}\left[\cos(\tfrac{1}{2}\theta_1-2\alpha)-\frac{3-\kappa}{1+\kappa}\cos\tfrac{1}{2}\theta_1\right]\right.\\
&\qquad\qquad\qquad\qquad \left. -r_2^{1/2}\left[\cos(\tfrac{1}{2}\theta_2+2\alpha)-\frac{3-\kappa}{1+\kappa}\cos\tfrac{1}{2}\theta_2\right]\right\}\\
&\quad -\frac{K_{\mathrm{II}}}{\sqrt{2\pi}}\cdot\frac{b_{11}\lambda^{-1/2}}{\cos\alpha}\left\{ r_1^{1/2}\left[\cos(\tfrac{1}{2}\theta_1-\alpha)-\frac{3-\kappa}{1+\kappa}\cos(\tfrac{1}{2}\theta_1+\alpha)\right]\right.\\
&\qquad\qquad\qquad\qquad \left. +r_2^{1/2}\left[\cos(\tfrac{1}{2}\theta_2+\alpha)-\frac{3-\kappa}{1+\kappa}\cos(\tfrac{1}{2}\theta_2-\alpha)\right]\right\},
\end{aligned}
\right\}
\tag{48}
$$

where

$$
\left.
\begin{aligned}
r_{1,2} &= r\left\{\left(\cos\theta\pm\lambda^{-1/4}\sqrt{\frac{1-\rho}{2}}\sin\theta\right)^2+\lambda^{-1/2}\left(\frac{1+\rho}{2}\right)\sin^2\theta\right\}^{1/2},\\
\theta_{1,2} &= \tan^{-1}\left\{\lambda^{-1/4}\sqrt{\frac{1+\rho}{2}}\left(1\pm\lambda^{-1/4}\sqrt{\frac{1-\rho}{2}}\tan\theta\right)^{-1}\tan\theta\right\},\\
\alpha &= \tan^{-1}\sqrt{\frac{1+\rho}{1-\rho}}.
\end{aligned}
\right\}
$$

Finally, for $\rho = 1$, the most singular stress components are

$$
\left.
\begin{aligned}
\sigma_{11} &= \frac{K_{\mathrm{I}}}{\sqrt{2\pi}} \cdot \frac{\lambda^{-1/2}}{r_1^{1/2}} \cos \tfrac{1}{2}\theta_1 (1 - \sin \tfrac{1}{2}\theta_1 \sin \tfrac{3}{2}\theta_1) \\
&\quad - \frac{K_{\mathrm{II}}}{\sqrt{2\pi}} \cdot \frac{\lambda^{-1/4}}{r_1^{1/2}} \sin \tfrac{1}{2}\theta_1 (2 + \cos \tfrac{1}{2}\theta_1 \cos \tfrac{3}{2}\theta_1), \\
\sigma_{22} &= \frac{K_{\mathrm{I}}}{\sqrt{2\pi}} \cdot \frac{1}{r_1^{1/2}} \cos \tfrac{1}{2}\theta_1 (1 + \sin \tfrac{1}{2}\theta_1 \sin \tfrac{3}{2}\theta_1) \\
&\quad + \frac{K_{\mathrm{II}}}{\sqrt{2\pi}} \cdot \frac{1}{\lambda^{-1/4} r_1^{1/2}} \sin \tfrac{1}{2}\theta_1 \cos \tfrac{1}{2}\theta_1 \cos \tfrac{3}{2}\theta_1, \\
\sigma_{12} &= \frac{K_{\mathrm{I}}}{\sqrt{2\pi}} \cdot \frac{\lambda^{-1/4}}{r_1^{1/2}} \sin \tfrac{1}{2}\theta_1 \cos \tfrac{1}{2}\theta_1 \cos \tfrac{3}{2}\theta_1 \\
&\quad + \frac{K_{\mathrm{II}}}{\sqrt{2\pi}} \cdot \frac{1}{r_1^{1/2}} \cos \tfrac{1}{2}\theta_1 (1 - \sin \tfrac{1}{2}\theta_1 \sin \tfrac{3}{2}\theta_1),
\end{aligned}
\right\}
\tag{49}
$$

and the displacement field is

$$
\left.
\begin{aligned}
u_1 &= \frac{K_{\mathrm{I}}}{\sqrt{2\pi}} \cdot \frac{4b_{11}\lambda^{-1/2}}{1+\kappa} r_1^{1/2} \cos \tfrac{1}{2}\theta_1 (\kappa - 1 + 2\sin^2 \tfrac{1}{2}\theta_1) \\
&\quad + \frac{K_{\mathrm{II}}}{\sqrt{2\pi}} \cdot \frac{4b_{11}\lambda^{-1/4}}{1+\kappa} r_1^{1/2} \sin \tfrac{1}{2}\theta_1 (\kappa + 1 + 2\cos^2 \tfrac{1}{2}\theta_1), \\
u_2 &= \frac{K_{\mathrm{I}}}{\sqrt{2\pi}} \cdot \frac{4b_{11}\lambda^{-3/4}}{1+\kappa} r_1^{1/2} \sin \tfrac{1}{2}\theta_1 (\kappa + 1 - 2\cos^2 \tfrac{1}{2}\theta_1) \\
&\quad - \frac{K_{\mathrm{II}}}{\sqrt{2\pi}} \cdot \frac{4b_{11}\lambda^{-1/2}}{1+\kappa} r_1^{1/2} \cos \tfrac{1}{2}\theta_1 (\kappa - 1 - 2\sin^2 \tfrac{1}{2}\theta_1),
\end{aligned}
\right\}
\tag{50}
$$

where

$$
r_1 = r\{\cos^2 \theta + \lambda^{-1/2} \sin^2 \theta\}^{1/2}, \qquad \theta_1 = \tan^{-1}(\lambda^{-1/4} \tan \theta).
$$

Notice that when, in addition to ρ, $\lambda = 1$, (49) and (50) will become identical to those obtained for isotropic materials.

B. Angular functions used in Section 3

In Section 3.1, the in-plane gradients of the out-of-plane displacement $u_3(x_1, x_2)$ are expressed in terms of the angular functions $F_{\alpha\beta}(\theta)$ ($\alpha, \beta = 1, 2$). For $\rho \neq 1$, these angular functions are given by

$$
\left.
\begin{aligned}
F_{11}(\theta) &= \mathrm{Re}\left\{\frac{\mu_2}{\mu_1 - \mu_2} \cdot \frac{b_{31}\mu_1^2 + b_{32}}{(\cos\theta + \mu_1\sin\theta)^{3/2}} - \frac{\mu_1}{\mu_1 - \mu_2} \cdot \frac{b_{31}\mu_2^2 + b_{32}}{(\cos\theta + \mu_2\sin\theta)^{3/2}}\right\}, \\
F_{12}(\theta) &= \mathrm{Re}\left\{\frac{1}{\mu_1 - \mu_2} \cdot \frac{b_{31}\mu_1^2 + b_{32}}{(\cos\theta + \mu_1\sin\theta)^{3/2}} - \frac{1}{\mu_1 - \mu_2} \cdot \frac{b_{31}\mu_2^2 + b_{32}}{(\cos\theta + \mu_2\sin\theta)^{3/2}}\right\}, \\
F_{22}(\theta) &= \mathrm{Re}\left\{\frac{\mu_1}{\mu_1 - \mu_2} \cdot \frac{b_{31}\mu_1^2 + b_{32}}{(\cos\theta + \mu_1\sin\theta)^{3/2}} - \frac{\mu_2}{\mu_1 - \mu_2} \cdot \frac{b_{31}\mu_2^2 + b_{32}}{(\cos\theta + \mu_2\sin\theta)^{3/2}}\right\},
\end{aligned}
\right\} \tag{51}
$$

and $F_{21}(\theta) = -\lambda^{-1/2}F_{12}(\theta)$ by noting the fact that $\mu_1\mu_2 = -\lambda^{-1/2}$. To be more explicit, consider the three cases for the parameter ρ separately.

For $\rho > 1$, the angular functions can be expressed as

$$
\left.
\begin{aligned}
F_{11}(\theta) &= \frac{\rho_-}{\rho_+ - \rho_-} \cdot \frac{b_{32} - \lambda^{-1/2}\rho_+^2 b_{31}}{h_+(\theta)} \cos\{\tfrac{3}{2}\tan^{-1}(\lambda^{-1/4}\rho_+\tan\theta)\} \\
&\quad - \frac{\rho_+}{\rho_+ - \rho_-} \cdot \frac{b_{32} - \lambda^{-1/2}\rho_-^2 b_{31}}{h_-(\theta)} \cos\{\tfrac{3}{2}\tan^{-1}(\lambda^{-1/4}\rho_-\tan\theta)\}, \\
F_{12}(\theta) &= -\frac{1}{\lambda^{-1/4}(\rho_+ - \rho_-)} \cdot \frac{b_{32} - \lambda^{-1/2}\rho_+^2 b_{31}}{h_+(\theta)} \sin\{\tfrac{3}{2}\tan^{-1}(\lambda^{-1/4}\rho_+\tan\theta)\} \\
&\quad + \frac{1}{\lambda^{-1/4}(\rho_+ - \rho_-)} \cdot \frac{b_{32} - \lambda^{-1/2}\rho_-^2 b_{31}}{h_-(\theta)} \sin\{\tfrac{3}{2}\tan^{-1}(\lambda^{-1/4}\rho_-\tan\theta)\}, \\
F_{22}(\theta) &= \frac{\rho_+}{\rho_+ - \rho_-} \cdot \frac{b_{32} - \lambda^{-1/2}\rho_+^2 b_{31}}{h_+(\theta)} \cos\{\tfrac{3}{2}\tan^{-1}(\lambda^{-1/4}\rho_+\tan\theta)\} \\
&\quad - \frac{\rho_-}{\rho_+ - \rho_-} \cdot \frac{b_{32} - \lambda^{-1/2}\rho_-^2 b_{31}}{h_-(\theta)} \cos\{\tfrac{3}{2}\tan^{-1}(\lambda^{-1/4}\rho_-\tan\theta)\},
\end{aligned}
\right\} \tag{52}
$$

where

$$
h_\pm(\theta) = (\cos^2\theta + \lambda^{-1/2}\rho_\pm^2\sin^2\theta)^{3/4},
$$

and $\rho_\pm$ has been defined in the previous section.

For $-1 < \rho < 1$, the angular functions are given by

$$
\begin{aligned}
F_{11}(\theta) &= -\frac{1}{2h_1(\theta)}\sqrt{\frac{2}{1-\rho}}\{b_{32}\cos(\tfrac{3}{2}\theta_1 + \alpha) + \lambda^{-1/2}b_{31}\cos(\tfrac{3}{2}\theta_1 - \alpha)\} \\
&\quad -\frac{1}{2h_2(\theta)}\sqrt{\frac{2}{1-\rho}}\{b_{32}\cos(\tfrac{3}{2}\theta_2 - \alpha) + \lambda^{-1/2}b_{31}\cos(\tfrac{3}{2}\theta_2 + \alpha)\}, \\
F_{12}(\theta) &= \frac{1}{2\lambda^{-1/4}h_1(\theta)}\sqrt{\frac{2}{1-\rho}}\{b_{32}\cos\tfrac{3}{2}\theta_1 + \lambda^{-1/2}b_{31}\cos(\tfrac{3}{2}\theta_1 - 2\alpha)\} \\
&\quad -\frac{1}{2\lambda^{-1/4}h_2(\theta)}\sqrt{\frac{2}{1-\rho}}\{b_{32}\cos\tfrac{3}{2}\theta_2 + \lambda^{-1/2}b_{31}\cos(\tfrac{3}{2}\theta_2 + 2\alpha)\}, \\
F_{22}(\theta) &= \frac{1}{2h_1(\theta)}\sqrt{\frac{2}{1-\rho}}\{b_{32}\cos(\tfrac{3}{2}\theta_1 - \alpha) + \lambda^{-1/2}b_{31}\cos(\tfrac{3}{2}\theta_1 - 3\alpha)\} \\
&\quad +\frac{1}{2h_2(\theta)}\sqrt{\frac{2}{1-\rho}}\{b_{32}\cos(\tfrac{3}{2}\theta_2 + \alpha) + \lambda^{-1/2}b_{31}\cos(\tfrac{3}{2}\theta_2 + 3\alpha)\},
\end{aligned}
\tag{53}
$$

where

$$
h_{1,2}(\theta) = \left\{\left(\cos\theta \pm \lambda^{-1/4}\sqrt{\frac{1-\rho}{2}}\sin\theta\right)^2 + \lambda^{-1/2}\left(\frac{1+\rho}{2}\right)\sin^2\theta\right\}^{3/4},
$$

and $\theta_{1,2}$ have been defined in the previous section.

Finally, for $\rho = 1$, the angular functions are

$$
\begin{aligned}
F_{11}(\theta) &= -\frac{\lambda^{-1/2}b_{31} + b_{32}}{4h(\theta)}\{(4 - 3\eta)\cos\tfrac{3}{2}\theta_1 + 3\eta\cos\tfrac{7}{2}\theta_1\}, \\
F_{12}(\theta) &= \frac{\lambda^{-1/2}b_{31} + b_{32}}{4\lambda^{-1/4}h(\theta)}\{(4 + \eta)\sin\tfrac{3}{2}\theta_1 + 3\eta\sin\tfrac{7}{2}\theta_1\}, \\
F_{22}(\theta) &= -\frac{\lambda^{-1/2}b_{31} + b_{32}}{4h(\theta)}\{(4 + 5\eta)\cos\tfrac{3}{2}\theta_1 + 3\eta\cos\tfrac{7}{2}\theta_1\},
\end{aligned}
\tag{54}
$$

where

$$
h(\theta) = (\cos^2\theta + \lambda^{-1/2}\sin^2\theta)^{3/4}, \qquad \theta_1 = \tan^{-1}(\lambda^{-1/4}\tan\theta),
$$

$$
\eta = \frac{\lambda^{-1/2}b_{31} - b_{32}}{\lambda^{-1/2}b_{31} + b_{32}}.
$$

More specifically, for $\lambda = 1$, one can show that

$$
F_{11}(\theta) = F_{22}(\theta) = \frac{2\nu}{E}\cos\tfrac{3}{2}\theta, \qquad F_{12}(\theta) = -F_{21}(\theta) = -\frac{2\nu}{E}\sin\tfrac{3}{2}\theta,
$$

where ν and E are the Poisson's ratio and Young's modulus, respectively, for the degenerate isotropic elastic material.

C. Stress intensity factor for the four-point-bend specimen

The stress intensity factor for an isotropic single-edge-notch specimen under pure bending load is given by

$$K_{\mathrm{I}} = \sigma \sqrt{\pi a} \cdot F\left(\frac{a}{b}\right), \tag{55}$$

where $F(a/b)$ is a function that only depends on the ratio a/b. $F(a/b)$ can be approximated by the following expression (Tada et al., 1985)

$$F\left(\frac{a}{b}\right) = \left(\frac{2b}{\pi a} \sin \frac{\pi a}{2b}\right)^{1/2} \left(\cos \frac{\pi a}{2b}\right)^{-3/2} \left\{0.923 + 0.199\left(1 - \sin \frac{\pi a}{2b}\right)^4\right\}.$$

The σ in (55) is related to the applied moment per unit thickness, M, through

$$\sigma = \frac{6M}{b^2}, \qquad M = \frac{Q}{2h}(l_2 - l_1),$$

where Q is the total force applied on the four-point-bend specimen and h is the specimen thickness. l_1 and l_2 are the half span of the top and the bottom loading pins. Substituting into (55), we have

$$K_{\mathrm{I}} = 3\sqrt{\pi}\frac{Q\left(l_2 - l_1\right)}{b^{3/2}h}\left(\frac{a}{b}\right)^{1/2} F\left(\frac{a}{b}\right). \tag{56}$$

Acknowledgements

References

Bao, G., Ho, S., Suo, Z. and Fan, B. (1992). The role of material orthotropy in fracture specimens for composites. *International Journal of Solids and Structures* **29**, 1105–1116.

Bruck, H.A. and Rosakis, A.J. (1992). On the sensitivity of Coherent Gradient Sensing: Part I – A theoretical investigation of accuracy in fracture mechanics applications. *Optics and Lasers in Engineering* **17**, 83–101.

Bruck, H.A. and Rosakis, A.J. (1993). On the sensitivity of Coherent Gradient Sensing: Part II – An experimental investigation of accuracy in fracture mechanics applications. *Optics and Lasers in Engineering* **18**, 25–51.

Chai, H. (1990). Interlaminar shear fracture of laminated composites. *International Journal of Fracture* **43**, 117–131.

Davies P. and Benzeggagh M.L. (1989). Interlaminar mode-I fracture testing (Edited by K. Friedrich), *Application of Fracture Mechanics to Composite Materials*, Elsevier, New York, 81–112.

Hutchinson, J.W. and Suo, Z. (1992). Mixed mode cracking in layered materials (Edited by J.W. Hutchinson and T. Wu), *Advances in Applied Mechanics* **29**, 63–191.

Krishnaswamy, S., Tippur, H.V. and Rosakis, A.J. (1992). Measurement of transient crack tip deformation fields using the method of coherent gradient sensing. *Journal of the Mechanics and Physics of Solids* **40**, 339–372.

Lee, Y.J., Lambros, J. and Rosakis, A.J. (1996). Analysis of Coherent Gradient Sensing (CGS) by Fourier optics. *Optics and Lasers in Engineering* **25**, 25–53.

Lekhnitskii, S.G. (1968). *Anisotropic Plates* (Translated by S.W. Tsai and T. Cheron), Gordon & Breach Science Publishers, New York.

Liu, C., Huang, Y., Lovato, M.L. and Stout, M.G. (1996). Measurement of the fracture toughness of a fiber-reinforced composite using the Brazilian disk sample geometry. Los Alamos National Laboratory Report LA-UR-96-3845, 1996. To appear in the *International Journal of Fracture*.

Mason, J.J., Lambros, J. and Rosakis, A.J. (1992). The use of a coherent gradient sensor in dynamic mixed-mode fracture mechanics experiments. *Journal of the Mechanics and Physics of Solids* **40**, 641–661.

Muskhelishvili, N.I. (1953). *Some Basic Problems in the Mathematical Theory of Elasticity* (Translated by J.R.M. Radok), Noordhoff, Groningen, Holland.

Rosakis, A.J. (1993). Two optical techniques sensitive to gradients of optical path difference: The method of caustics and the coherent gradient sensor (CGS) (Edited by J. Epstein), *Experimental Techniques in Fracture* **3**, Chapter 10, 327–425.

Rosakis, A.J. (1994). Private communications.

Rosakis, A.J. and Ravi-Chandar, K. (1986). On crack-tip stress state: An experimental evaluation of three-dimensional effects. *International Journal of Solids and Structures* **22**, 121–134.

Sanford, R.J. and Dally, J.W. (1979). A general method for determining mixed-mode stress intensity factors from isochromatic fringe patterns. *Engineering Fracture Mechanics* **11**, 621–633.

Tada, H., Paris, P.C. and Irwin, G.R. (1985). *The Stress Analysis of Cracks Handbook*. Del Research, St. Louis, MO.

Tippur, H.V. (1992). Coherent gradient sensing: A Fourier optics analysis and applications to fracture. *Appl. Optics* **31**, 4428–4439.

Tippur, H.V., Krishnaswamy, S. and Rosakis, A.J. (1991). A coherent gradient sensor for crack tip measurements: Analysis and experimental results. *International Journal of Fracture* **48**, 193–204.

Yoon S.H. and Hong C.S. (1990). Interlaminar fracture toughness of graphite/epoxy composite under mixed-mode deformations. *Experimental Mechanics* **30**, 234–239.